

# Design and Experimental Validation of a Piezoelectric Resonant MEMS Phase Comparator

Mathieu Gratuze, *Member, IEEE*, Mohammad Kazemi, Seyedfakhreddin Nabavi, *Member, IEEE*  
Paul-Vahé Cicek, *Member, IEEE*, Alexandre Robichaud, *Member, IEEE*, and Frederic Nabki, *Member, IEEE*

**Abstract**—In this paper, the design, concept and experimental validation of the performances of a piezoelectric resonant microelectromechanical systems (MEMS) phase comparator is presented. Compared to traditional integrated circuits, the potential benefits of a MEMS phase comparator include a low power consumption, higher sensitivity, higher selectivity and improved robustness. The design and experimental validation of a resonant MEMS phase comparator are presented along with characterization recommendations. The operation of this resonant MEMS phase comparator is experimentally validated over the first five eigenmodes at 108 kHz, 298.7 kHz, 583.3 kHz, 962.8 kHz and 1.4375 MHz. Calibration of the resonant MEMS phase comparator is presented, allowing for simple device operation, which is validated under various waveform stimulations: sinusoidal, square, and triangular. This work is expected to lead to the development of new applications for MEMS resonating devices.

**Index Terms**—Piezo-electricity, Phase Comparator, Phase Detector, Mode Shape suppression, MEMS, Resonator, Signal Processing

## I. INTRODUCTION

**S**IGNAL processing has been achieved using micro-electromechanical systems (MEMS), as various instances have been proposed, including band-pass, high-pass, and low-pass filters, as well as resonators [1–3]. Phase comparators, also known as phase detectors, serve as crucial components in numerous electronic systems, notably in phase-locked loops (PLLs) [4]. They can also be encountered in diverse applications, such as motor control, radar and telecommunication systems, servo mechanisms, demodulators, and clock and data recovery circuits (CDRs) [4–7]. Phase comparators also allow information recovery from sensors, as in the cases of Coriolis flow meters, and Kelvin probe force microscopy (KPFM). In the former, the mass flow rate is directly proportional to the phase difference measured [8] while in the latter the phase difference between signals allows the measurement of the work function of surfaces [9], [10].

Since the first phase detectors were presented in the 1960s [11–13], various phase detector architectures have been presented in the literature [5–7], [14–16]. From a practical point

of view, phase detectors can be divided into two main classes: linear phase detector and binary phase detector (or Bang Bang phase detector) [4]. In the case of a linear phase detector, the transfer function is somewhat linear between the output and the input phase error, while a Bang Bang phase detector produces an error signal that corresponds to the sign of the instantaneous phase error [4].

When designing a phase detector, the integrated circuits (IC) designer is interested in providing a DC output signal which value varies as a function of the phase difference between the two inputs signals. This should be achieved within the smallest possible area, while minimizing power consumption. Another challenge is raised in reducing the size of the deadzone, which is the minimum phase difference that can be resolved by the phase detector [17].

MEMS devices have a high potential for integration with ICs, either inside, above, or beside the IC die [18–22]. Therefore, a MEMS phase comparator could occupy a minimal additional footprint, offering significant advantages from an IC designer's perspective. Furthermore, using a resonant MEMS device to execute phase comparison leverages the benefits offered by resonant sensors: excellent accuracy, sensitivity, stability [23], [24]. As such, this could lead the way to more compact, more efficient hybrid MEMS-IC Frequency Synthesizers [18].

However, to the best of the authors' knowledge, the literature on MEMS phase comparators is limited to the work of Dunk et al. [25], and that of Han et al. [26–30]. Work in [25] claims a device with the potential for higher sensitivity, higher selectivity, faster lock time, low power consumption, and improved robustness. It makes use of Huygens Synchronization, the mechanical phenomenon behind the synchronization of two hanging pendulums [31]. The work of Han et al. consists in a power combiner with a thermoelectric power sensor to achieve a broadband MEMS phase comparator, at a much higher frequency (i.e. from 8 GHz to 12 GHz). However, this comes at the cost of high power consumption (up to 1 W) [26].

This work is an extension of the results presented in [32], and thus targets a simpler structure to implement a piezoelectric resonant MEMS phase comparator: a clamped-clamped beam. The contributions of this work are:

- (i) design and experimental validation of a piezoelectric resonant MEMS phase comparator;
- (ii) formulation of recommendations on the characterization of MEMS phase comparators;

M. Gratuze, M. Kazemi, S. Nabavi and F. Nabki are with the Department of Electrical Engineering, École de Technologie Supérieure, Université du Québec, Montréal, QC H3C 1K3, Canada P-V. Cicek is with the Department of Software engineering, Université du Québec à Montréal, Montréal, QC H2X 3Y7, Canada A. Robichaud is with the Department of Applied Sciences, Université du Québec à Chicoutimi, Saguenay, QC G7H 2B1, Canada (e-mail: mathieu.gratuze.1@ens.etsmtl.ca; mohammad.kazemi.1@ens.etsmtl.ca; cicek.paul-vahe@uqam.ca; alexandre\_robichaud@uqac.ca; frederic.nabki@etsmtl.ca).

- (iii) experimental validation of the operation of the resonant MEMS phase comparator over a wide frequency range and a variety of waveforms;
- (iv) presentation of a simple calibration method for the operation of resonant MEMS phase comparators.

Accordingly, this work explores the use of a MEMS resonator to act as a phase comparator. The necessary background and simulations are presented in Section II, followed by experimental validation in Section III, which covers design and fabrication of the devices, experimental test setup and experimental results. Thereafter, Section IV provides a discussion of the use of a resonant MEMS phase comparator. Finally, conclusions are presented in Section V.

## II. OPERATING PRINCIPLE

It is well known that electrode placement has an impact on the behavior of a MEMS resonator. Researchers have proposed methods to improve electrode configuration, thereby increasing the energy generated by MEMS vibrational energy harvesters [33], [34]. Likewise, employing dual electrodes has been shown to enhance the performance of MEMS devices. Such a configuration has been used in [35] to improve the performance of piezoelectric micromachined ultrasonic transducers (PMUTs), in [36] to improve the performance of a MEMS microspeaker and in [1] to improve the performance of a MEMS resonator. In this study, the electrode placement has been designed to emulate methods used in coupling MEMS resonators. This approach aims to enable measurement of the phase difference between two different excitation signals. Such coupled resonators have been proposed in the literature to improve the sensibility of MEMS resonators for sensing and timing applications [37–39].

The behavior of clamped-clamped beams has been extensively studied in the literature [40–43]. Analytically, the resonant frequency  $f_0$  of a clamped-clamped beam depends on its length,  $L$ , thickness,  $H$ , equivalent Young's modulus  $E_{eq}$ , and material's density,  $\rho_{eq}$ . It can be estimated as [43]:

$$f_0 = 1.03 \frac{H}{L^2} \sqrt{\frac{E_{eq}}{\rho_{eq}}} \quad (1)$$

However, this paper does not aim to explore or introduce new or improved modeling methods for clamped-clamped beams. Thus, the resonant frequency, mode shape, and simulation of the behavior of the resonant MEMS phase comparator has been performed using finite element methods (FEM) with the COMSOL Multiphysics software (version 5.5).

This paper studies a phase comparator that is a clamped-clamped beam resonator, featuring two electrodes, each covering one half of the beam. The dimensions of the simulated MEMS are presented in detail in Table I. The materials and dimensions are consistent with the ones available in the commercial PiezoMUMPs process from MEMSCAP (Crolles, France) since this process is used for the fabrication of the prototypes in this work. The intrinsic properties of the materials (Si, SiO<sub>2</sub>, AlN, Al) used in this simulation including density, Young's modulus, are obtained from the material library of the COMSOL Multiphysics software. The damping in the

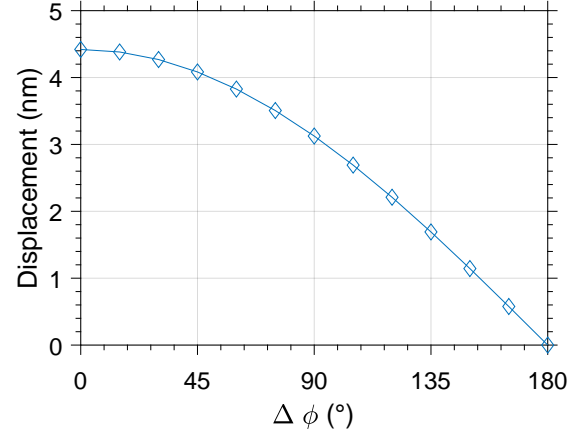


Fig. 1: Simulation of the influence of  $\Delta\varphi$  on the displacement of the central point of the resonator.

resonator has been simulated using a straightforward isotropic factor loss which has been fine-tuned using the experimentally gathered data to a value of 0.0064.

As the aim of this work is to present the operation of the resonant MEMS phase comparator, two excitation signals, using the waveform function of COMSOL, have been defined ( $F_{S1}$  and  $F_{S2}$ ) as follows:

$$F_{S1}(t) = \frac{A}{2} \sin(2\pi f_e t + \varphi_1) \quad (2)$$

$$F_{S2}(t) = \frac{A}{2} \sin(2\pi f_e t + \varphi_2) \quad (3)$$

where,  $A$  is the peak to peak amplitude of the excitation signal in V,  $f_e$  denotes the frequency of the excitation signal in Hz, and  $\varphi_1$  and  $\varphi_2$  are the phases of each signal in °. The phase difference  $\Delta\varphi$  between these two signals is equal to  $\varphi_2 - \varphi_1$ . To simplify and reduce the number of simulations, the value of  $\varphi_1$  was set to 0°, and thus  $\Delta\varphi$  is equal to  $\varphi_2$  in practice.

Using the parametric sweep feature of the time domain study, it is possible to extract the effect of  $\Delta\varphi$  on the amplitude of the displacement of the central point of the resonator, as shown in Fig. 1.

Fig. 2 illustrates the variation of the amplitude of the displacement of the central point of the simulated MEMS resonator: if  $\Delta\varphi$  is equal to 0 degree, the central point corresponds to a local maximum of displacement (see Fig. 2a). However, if  $\Delta\varphi$  is equal to 180 degree, no displacement occurs

TABLE I: Overview of the dimensions of the device.

Type	Clamped-Clamped
Beam length (μm)	800
Beam width (μm)	100
Beam thickness (μm)	10
AlN thickness (μm)	0.5
Electrode thickness (μm)	1.02
Separation of the electrodes (μm)	5
Number of electrodes	2

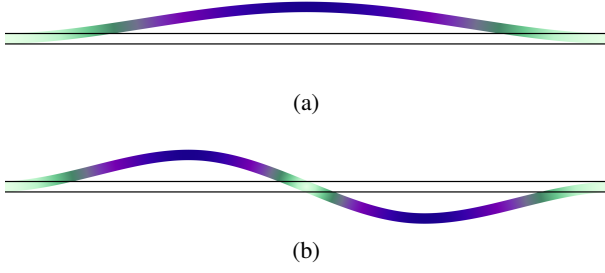


Fig. 2: Simulation of the mode shape of the resonant MEMS phase comparator,  $\Delta\varphi$  is equal to (a)  $0^\circ$ , (b)  $180^\circ$ .

at the central point, as it corresponds to a node of the mode shape (see Fig. 2b).

### III. EXPERIMENTAL VALIDATION

#### A. Design and Fabrication

The fabrication layout of the resonator was scripted in the SKILL language with the Cadence Virtuoso layout tool. This parameterized cell (PCell), which describes the devices' layout, facilitates easy scaling and variation of design parameters while ensuring compliance with design rules. Fig. 3 shows both the top view and cross section of the layout of the device. The prototypes were fabricated using the PiezoMUMPs technology from MEMSCAP. This process is a piezoelectric-based MEMS process that provides cost-effective access to MEMS prototyping. Since its introduction in 2013, this technology has been used for the creation of several resonators, actuators, ultrasonic transducers and energy harvesters [44–47]. The process includes five masks and is carried out on an N-type double-side polished silicon-on-insulator (SOI) wafer. The  $10\mu\text{m}$ -thick silicon (Si) layer is doped to increase its conductivity. This layer of doped silicon will act as the bottom electrode. Subsequently, a  $0.2\mu\text{m}$ -thick insulating layer of silicon dioxide ( $\text{SiO}_2$ ) is grown and patterned on the SOI wafer. A  $0.5\mu\text{m}$ -thick piezoelectric layer of aluminum nitride (AlN) is then deposited and patterned. Subsequently, a layer of metal consisting of a stack of  $0.02\mu\text{m}$ -thick chromium (Cr) and of  $1\mu\text{m}$ -thick aluminum (Al) is deposited followed by the patterning of the silicon device layer. Finally, the  $400\mu\text{m}$ -thick substrate is etched from the backside to create the bottom trench of the structure, releasing the proof mass and enabling movement. For more information on this fabrication process, [48] comprehensively describes the PiezoMUMPS process and its design rules.

A micrograph of the fabricated piezoelectric resonant MEMS phase comparator proposed in this work is shown in Fig. 4. In the micrograph, three measurement points are identified, one in the middle of the cantilever (red) and two at each quarter point (blue and green). The dimensions of the fabricated MEMS are presented in Table I.

#### B. Description of the Experimental Test Setup

A laser vibrometer was used for experimental measurement. This instrument can detect the velocity of any single point of

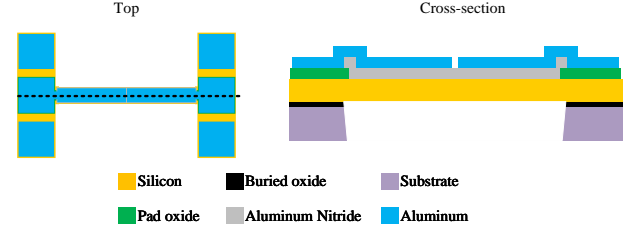


Fig. 3: Top view and cross section of the fabrication process used to implement the resonant MEMS phase comparator.

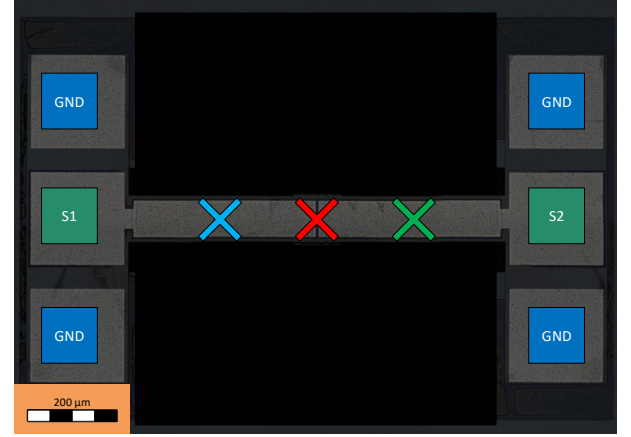


Fig. 4: Micrograph of the fabricated resonant MEMS phase comparator, both electrodes pads are labelled (S1, S2) along with the central (red), left (blue) and right (green) velocity measurement points.

the resonant MEMS phase comparator without the need for mechanical contact, using the test setup depicted in Fig. 5. This instrument was acquired from Polytec, (Irvine, CA, USA). Excitation of the resonant MEMS phase comparator is provided using a function generator type AFG3252 from Tektronix (Beavertown, Or, USA), which can provide dual output signals with a controllable phase difference. Channels 1 and 2 are respectively connected to the S1 and S2 pads which are shown in Fig. 4, with the underlying beam grounded.

Velocity measurements were taken at 3 different points: right, center, and left as shown in Fig. 4: the central point is used for odd Eigen modes while the left and right points are used for even Eigen modes. To satisfy the Nyquist-Shannon sampling theorem, the sampling frequency  $F_s$  was adjusted for each test. All discussed excitation voltage amplitudes are reported as their peak-to-peak values.

Considering that a clamped-clamped beam resonator can behave non-linearly [49], and that the resonant MEMS phase comparator will be excited by an excitation signal containing a single frequency, the recommendations made by [50] have been followed and the resonant MEMS phase comparator has been characterized using a pulsed sweep type excitation. The resonant frequency and operating bandwidth for the first five Eigen modes have been extracted and are presented in Table II.

As stated in section II, the resonant frequency has been simulated using COMSOL Multiphysics, version 5.5. The measured resonant frequency corresponds to the frequency

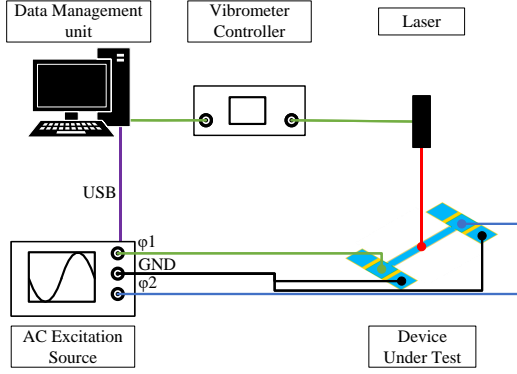


Fig. 5: Schematic of the test bench using a vibrometer and a double channel function generator.

at which the maximum velocity of the measured point(s) was achieved. The operating bandwidth has been defined as the frequency range in which the amplitude of the measured velocity is greater or equal to 50% of the maximum velocity.

### C. Consideration on the characterization of a resonant MEMS phase comparator

The goal of this work is to present the operation of a resonant MEMS phase comparator. As such, the excitation signal from channel 1 ( $F_{S1}(t)$ ) has been set as in 2, with  $\varphi_1 = 0$ , and the excitation signal from channel 2 ( $F_{S2}(t)$ ) as in 3, thus  $\varphi_2 = \Delta\varphi$ . Channel 1 and 2 are applied to pads S1 and S2, respectively.

The behavior of the MEMS is non-linear, hysteresis will influence the measurement results. To quantify this hysteresis, the MEMS resonator was excited by using three different excitation voltage signals, namely:

- pulsed phase sweep (PPS), where the value of  $\Delta\varphi$  is discretely swept,
- continuous phase sweep forward (CPSF), where the value of  $\Delta\varphi$  is swept in a continuously ascending manner,

TABLE II: Summary of the resonance characteristics when the amplitude of the excitation signal is equal to 10 V.

Eigen-mode	Parameter	Value
1 <sup>st</sup>	Simulated Resonant Frequency (kHz)	103.4
	Measured Resonant Frequency (kHz)	108.6
	Operating Bandwidth (kHz)	107.5 — 108.75
2 <sup>nd</sup>	Simulated Resonant Frequency (kHz)	284.6
	Measured Resonant Frequency (kHz)	298.7
	Operating Bandwidth (kHz)	295.8 — 299.45
3 <sup>rd</sup>	Simulated Resonant Frequency (kHz)	558.3
	Measured Resonant Frequency (kHz)	583.2
	Operating Bandwidth (kHz)	581.0 — 583.35
4 <sup>th</sup>	Simulated Resonant Frequency (kHz)	922.9
	Measured Resonant Frequency (kHz)	962.8
	Operating Bandwidth (kHz)	960.4 — 964.80
5 <sup>th</sup>	Simulated Resonant Frequency (kHz)	1378.9
	Measured Resonant Frequency (kHz)	1437.5
	Operating Bandwidth (kHz)	1433.2 — 1440.8

- continuous phase sweep backward (CPSB), where the value of  $\Delta\varphi$  is swept in a continuously descending manner,

The nature of these three excitation signals is similar to the sweep in frequency used in [50]. However, in this case, the sweep is affecting the value of  $\Delta\varphi$  and the frequency of the excitation signal is kept constant at  $f_e$ .

When excited with a PPS type excitation, the MEMS device is excited at a particular value of  $\Delta\varphi$ , for a given duration of  $T_{on}$ ; afterwards, the excitation is paused for the duration of  $T_{off}$ . The value of  $\Delta\varphi$  is sequentially swept between  $\Delta\varphi_{start}$  and  $\Delta\varphi_{end}$ , the lowest and highest targeted phase differences, respectively. The phase difference is thus discretized with the PPS excitation resolution of ( $\Delta\varphi_{res}$ ) equal to:

$$\Delta\varphi_{res} = \left| \frac{\Delta\varphi_{end} - \Delta\varphi_{start}}{Nb_{meas}} \right| \quad (4)$$

where  $Nb_{meas}$  is the number of performed measurements. It has been experimentally validated that if the duration of  $T_{off}$  is long enough that the vibration of the resonant MEMS phase comparator is extinguished between 2 excitations, the sequence of the excitation of  $\Delta\varphi$  does not have an influence on the experimental results.  $T_{on}$  and  $T_{off}$  are clearly labeled in Fig. 6(a) for the PPS excitation signal.

An example of the PPS type excitation is shown in Fig. 6(a), where the amplitude of the excitation signal,  $A$  is set to 10 V, the frequency of the excitation  $f_e$  is 200 kHz, the duration of  $T_{on}$  and  $T_{off}$  are equal to 10  $\mu$ s each, while  $\Delta\varphi_{start}$  and  $\Delta\varphi_{end}$  are 0° and 180° respectively and  $Nb_{meas}$  is set to 5, resulting in  $\Delta\varphi_{res} = 45^\circ$ .

CPSF and CPSB excitations are similar in nature. For both excitation types, similarly to PPS excitation, the value of  $\Delta\varphi$  is sequentially swept between  $\Delta\varphi_{start}$  and  $\Delta\varphi_{end}$ . The measured phase difference is thus discrete and the resolution of CPSF excitation ( $\Delta\varphi_{res}$ ) is equal to the one of the PPS type excitation.

Thus, when excited with the CPSF or CPSB excitations, the MEMS device is subjected to a particular value of  $\Delta\varphi$ , for a given duration of  $T_{on}$ ; afterwards the value of  $\Delta\varphi$  is gradually modified at a sweep rate  $S_R$  for a duration  $T_{var}$ . The difference between CPSF and CPSB type excitations lies in the sweep rate: positive for CPSF excitation and negative for CPSB excitation. The value of  $S_R$  is defined as:

$$S_R = \frac{\Delta\varphi_{end} - \Delta\varphi_{start}}{T_{var}} \quad (5)$$

An example of the CPSF and CPSB type excitation is shown in Fig. 6(b) and Fig. 6(c) respectively. In this case, the amplitude of the excitation signal  $A$  is set to 10 V, the frequency of the excitation  $f_e$  is 200 kHz, the duration of  $T_{on}$  and  $T_{var}$  are equal to 10  $\mu$ s, while  $\Delta\varphi_{start}$  and  $\Delta\varphi_{end}$  are 0° and 180° respectively,  $Nb_{meas}$  has been chosen to be equal to 5, thus resulting in  $\Delta\varphi_{res} = 45^\circ$  and the value of  $S_R$  is 4 500 000 ° s<sup>-1</sup> and -4 500 000 ° s<sup>-1</sup> for the CPSF and CPSB type excitation respectively.  $T_{on}$  and  $T_{var}$  are clearly labeled in Fig. 6(b) and Fig. 6(c) and for the CPSF and CPSB excitation signal respectively.



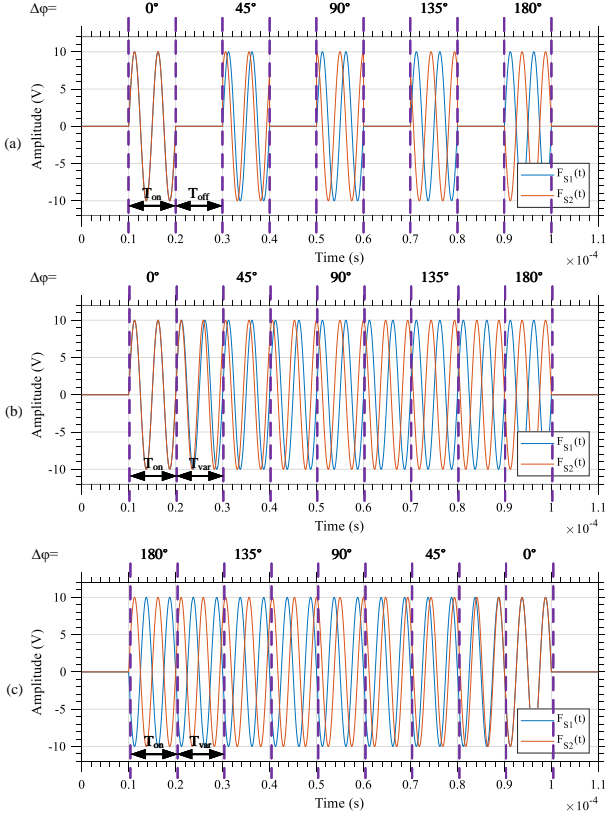


Fig. 6: Examples of 3 of the excitation signal types used: (a) Pulse Phase Sweep (PPS), (b) Continuous Phase Sweep Forward (CPSF) and (c) Continuous Phase Sweep Backward (CPSB).

It should be noted that, from a practical point of view, if there is a difference between the measurements obtained using the PPS, CPSF and CPSB type excitation, this value of  $S_R$  is too high for the frequency of the excitation  $f_e$  (200 kHz) as it results in a variation of 22.5° per period and would then result in non-repeatable results. From an experimental point of view, it is recommended to keep the value of  $S_R$  low enough so that the variation of  $\Delta\varphi$  is lower or equal to 0.5° per period such that:

$$S_R T_e = \frac{S_R}{f_e} \leq 0.5^\circ. \quad (6)$$

For the 1<sup>st</sup> Eigen mode, the central point has been chosen as the measurement location. The three types of excitations (PPS, CPSF and CPSB) have been used to characterize the influence of the variation of  $\Delta\varphi$ , when  $f_e = 108$  kHz. This characterization has first been performed for an amplitude of 10 V peak-to-peak, which is shown in Fig. 7a. In this figure, the impact of the excitation type can be seen. While the results obtained for  $\Delta\varphi = 0^\circ$  or  $\Delta\varphi = 180^\circ$  are the same for all three excitation types, the same is not true when  $\Delta\varphi = 90^\circ$ . This same characterization has then been performed with a smaller amplitude of 2.5 V peak-to-peak, as shown in Fig. 7b. In this case, the results are now consistent with the simulation results previously shown in Fig. 1.

It is clear that the influence of the type of excitation (CPSF, CPSB, PPS) on the measured RMS velocity at low excitation amplitudes is negligible. Nonetheless, in order to reduce the impact of hysteresis going forward, the characterization has been performed using PPS type excitation.

It should be noted that a discontinuity in the phase response of the resonant MEMS phase comparator can be observed, in Fig. 7a, when  $\Delta\varphi$  is equal to 70°, 90° and 10° for the PPS, CPSF and CPSB type excitations, respectively. However, since such a discontinuity does not appear in Fig. 7b, this discontinuity is thus attributed to the nonlinearity of the resonant MEMS phase comparator.

The influence of the amplitude of the excitation signal ( $A$ ) on the frequency response of the MEMS resonator is presented  $\Delta\varphi = 0^\circ$  in Fig. 8a. In this figure, the non-linearity of the resonator for larger amplitudes of actuation is clearly visible, justifying the choice of pulsed sweep excitation in order to carry-out subsequent measurements, and also confirming the non-linear effect observed in Fig. 7a.

#### D. Operation of the resonant MEMS phase comparator at the first Eigen mode

Fig. 8b shows the effect of both amplitude ( $A$ ) of the excitation signal and variation of  $\Delta\varphi$  (PPS excitation) between 0° and 360° on the RMS velocity of the central point of the device. In this measurement, the excitation frequency  $f_e$  is equal to 108 kHz, close to the first Eigen mode. It is clear that the RMS velocity of the central point can be used as a proxy to measure the phase difference between  $F_{S1}$  and  $F_{S2}$ . Indeed, the maximum RMS velocity is reached when  $\Delta\varphi$  approaches 0° or 360°, but is minimal when  $\Delta\varphi$  approaches 180°. It is also apparent that it is impossible to determine which signal leads the other, as the measured RMS velocity is the same if  $\Delta\varphi = 90^\circ$  or if  $\Delta\varphi = 270^\circ$ .

To validate the operating principle of the resonant MEMS phase comparator, the test setup shown in Fig. 5, along with two positioners and a positioning controller from Physik Instrumente (PI) (Karlsruhe, Germany), has been used to acquire heat maps of the RMS velocity of the resonant MEMS phase comparator. For both measurements, the amplitude  $A$  and frequency of the excitation signal  $f_e$  are set to 10 V and

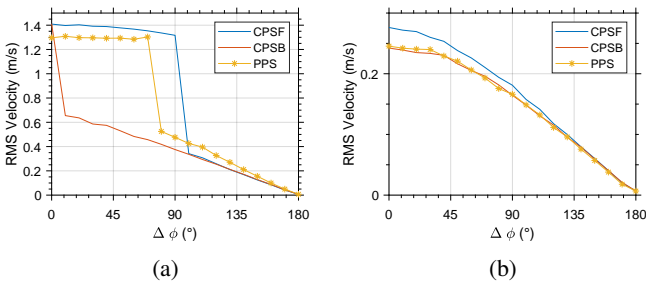


Fig. 7: Influence of the hysteresis of the MEMS resonator on the RMS velocity at the central point,  $f_e = 108$  kHz, when the amplitude of the excitation signal  $A$  is equal to (a) 10 V and (b) 2.5 V.

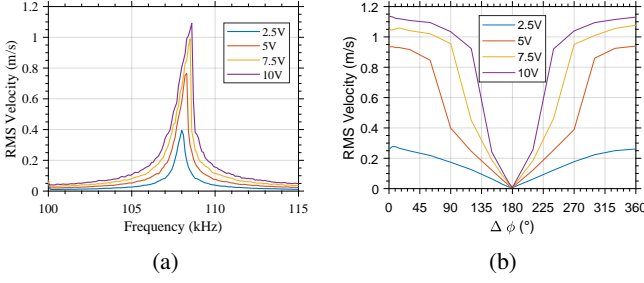


Fig. 8: For the 1<sup>st</sup> Eigen mode, at the central point, (a) frequency response of the MEMS ( $\Delta\varphi = 0^\circ$ ), (b) influence of the variation of  $\Delta\varphi$  on the RMS velocity when  $f_e = 108$  kHz.

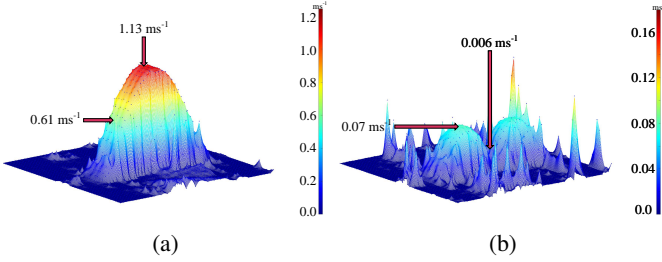


Fig. 9: Visualization of the heat-map of the RMS velocity of the resonant MEMS phase comparator, with  $A = 10$  V,  $f_e = 108$  kHz and  $\Delta\varphi$  is equal to (a)  $0^\circ$ , (b)  $180^\circ$ .

108 kHz respectively. For the first measurement,  $\Delta\varphi$  is set to  $0^\circ$  (see Fig. 9a) while, for the second measurement,  $\Delta\varphi$  is set to  $180^\circ$  (see Fig. 9b).

RMS velocity heat maps are coherent with the simulated mode shape of the beam as shown in Fig. 2. A heat map of the RMS velocity has been preferred over a visualization of the mode shape due to the low amplitudes of Fig. 9b which made the mode shape not a great visualization. To emphasize the low amplitude of Fig. 9b, scale arrows have been added to indicate the RMS velocity of the central and left quarter point.

It should be noted that the maximum RMS velocity, measured on the right and left measurement points of the beam (Fig. 9b ( $0.07 \text{ ms}^{-1}$ )) is about 16 times lower than the maximum RMS velocity measured on the beam in Fig. 9a ( $1.13 \text{ ms}^{-1}$ ). For  $\Delta\varphi$  equal  $0^\circ$ , the RMS velocity at the central point is about 190 times greater than when  $\Delta\varphi$  is equal to  $180^\circ$  ( $1.13 \text{ ms}^{-1}$  vs  $0.006 \text{ ms}^{-1}$ ). This validates the operation of the resonant MEMS phase comparator and also opens the way to the use of higher Eigen modes of the resonant MEMS phase comparator.

#### E. Operation of the resonant MEMS phase comparator for higher-order Eigen modes

The operation of the resonant MEMS phase comparator is not limited to the first Eigen mode. As such, its operation was also experimentally verified using higher order modes. Table III summarizes the experimental characterization of the device for the second to fifth Eigen modes. For each mode, the measurement point considered is indicated along with the

value of  $\Delta\varphi$  used to measure the frequency and phase response of the MEMS phase comparator. It should be noted that, although the central point corresponds to a local maximum displacement for odd Eigen modes, this is not the case for even Eigen modes, where the central point corresponds to a nodal point. Therefore, for even Eigen modes, the measurement points identified as left and right in Fig. 4 are used. Experimentally, it has been verified that both measurement points (i.e., left and right) exhibit similar behavior.

For each Eigen mode number 2 to 5, the mode shape of the MEMS resonator has been extracted when  $A = 10$  V and for  $\Delta\varphi = 0^\circ$  and when  $180^\circ$  and is shown in Table III. It should be noted that this representation is the actual mode shape of the device, which differs from the RMS velocity heatmap previously shown in Fig. 9a and Fig. 9b. Indeed, the advantage of a heatmap style visualization is to highlight the symmetry between the left and right measuring points. However when dealing with higher order Eigen modes (i.e. 3 to 5), this type of visualization actually hinders the ability of the reader to precisely identify the order of the Eigen mode which is being shown.

In the case of the higher order Eigen modes (i.e. 2 to 5) the suppressed mode shape is similar to the non-suppressed mode shape as it can be observed in Table III.

The difference between these mode shapes lies in the amplitude of the RMS velocity shown. In the case of the even Eigen mode (i.e. 2 and 4) the amplitude of the RMS velocity when  $\Delta\varphi$  is equal to  $180^\circ$  is about 118 and 46 times greater than when  $\Delta\varphi$  is equal to  $0^\circ$  for the second and fourth Eigen mode respectively.

In the case of the odd Eigen mode (i.e. 3 and 5) the amplitude of the RMS velocity when  $\Delta\varphi$  is equal to  $0^\circ$  is about 146 and 103 times greater than when  $\Delta\varphi$  is equal to  $180^\circ$  for the third and fifth Eigen mode respectively.

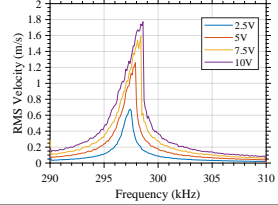
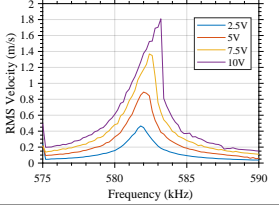
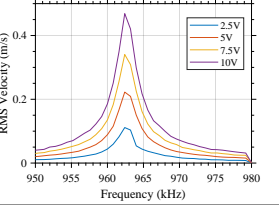
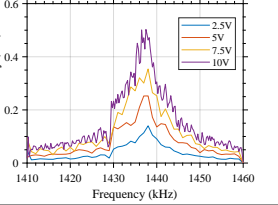
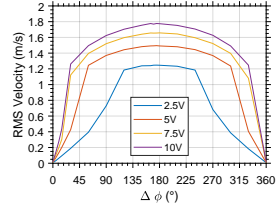
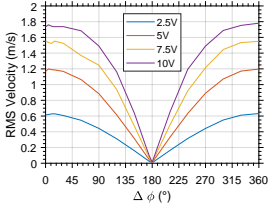
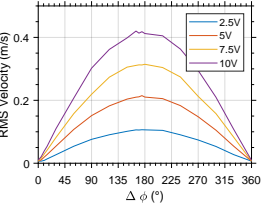
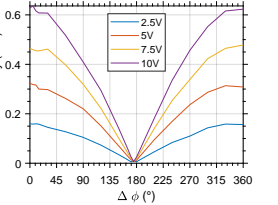
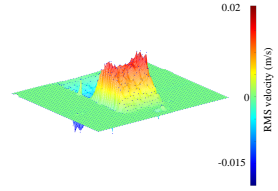
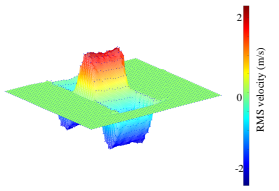
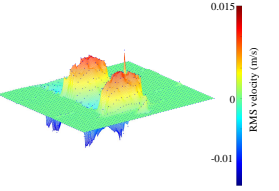
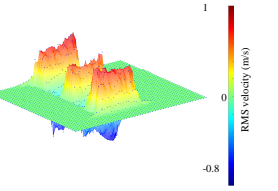
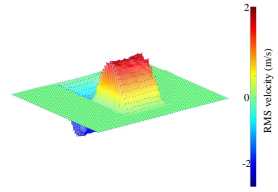
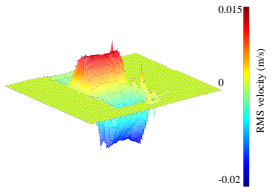
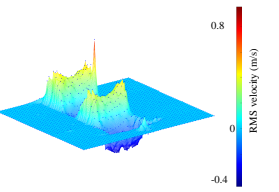
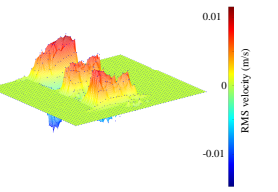
As evidenced by the mode shapes shown in Table III, the electrodes of the current MEMS resonator are not optimal to excite the mode shapes of the Eigen mode number 2 to 5.

It is interesting to note that the impact of the variation of  $\Delta\varphi$  on the RMS velocity of the resonant MEMS phase comparator varies as a function of the parity of the Eigen mode. For any  $k$  an integer belonging to  $\mathbb{Z}$ , for odd Eigen modes, a maximum RMS velocity is achieved when  $\Delta\varphi$  is equal to  $2k\pi$ . Conversely for even Eigen modes, this phase shift corresponds to the minimum RMS velocity. Similarly, when  $\Delta\varphi$  is equal to  $(2k+1)\pi$ , the minimal RMS velocity for odd Eigen modes is observed, while for even Eigen modes, the maximum RMS velocity is seen.

As was previously observed for the first Eigen mode, and regardless of the parity, it is impossible to determine which of the two electrical signals leads the other, since the measured RMS velocity is symmetrical over the  $\Delta\varphi$  range.

It is also noteworthy that the first two Eigen modes show a discontinuity in the phase response, these two modes are also the ones exhibiting a strong non linear frequency response thus further validating the hypothesis that this discontinuity is related to the non-linearity of the resonant MEMS phase comparator.

TABLE III: Summary of the impact of the phase difference on the measurements at higher Eigen modes (2 to 5).

Eigen mode	2	3	4	5
Measurement point	left / right	center	left / right	center
$\Delta\varphi$ Frequency response	180°	0°	180°	0°
Pulsed Frequency response				
$f_e$ (kHz)	297.4	581.8	962.8	1437.5
Pulsed Phase response				
Mode Shape when $\Delta\varphi = 0^\circ$				
Mode Shape when $\Delta\varphi = 180^\circ$				

### F. Calibration of the device

It has been previously noted that the relationship between measured displacement (or velocity) does not follow a linear relationship with respect to  $\Delta\varphi$ . Still, both simulation and experimental data show that it is possible to fit the measured displacement (or velocity). Extrapolating the actual velocity amplitude of the resonant MEMS phase comparator ( $V_{predicted}(\Delta\varphi)$ ) at a given frequency  $f_{meas}$ , excitation amplitude  $A_{meas}$  and  $\Delta\varphi$  only requires the extraction of the velocity amplitude at  $f_{meas}$  from the frequency response  $V_{f_{meas}}$  of the resonant MEMS phase comparator when the amplitude of the excitation signal is equal to  $A_{meas}$  which is then denoted  $V_{f_{meas}}(A_{meas})$ .

Then, the prediction depends on the parity of the Eigen mode: for odd modes, the estimated velocity for a given value of  $\Delta\varphi$ , and amplitude of the excitation signal denoted ( $V_{pred}(\Delta\varphi)$ ) can be estimated as:

$$V_{pred}(\Delta\varphi) = \left| V_{f_{meas}}(A_{meas}) \cos\left(\frac{\Delta\varphi}{2}\right) \right| \quad (7)$$

For even modes, it can be estimated as:

$$V_{pred}(\Delta\varphi) = \left| V_{f_{meas}}(A_{meas}) \sin\left(\frac{\Delta\varphi}{2}\right) \right| \quad (8)$$

Thus, using trigonometric properties, it is possible to define a global estimation function:

$$V_{pred}(\Delta\varphi) = \left| V_{f_{meas}}(A_{meas}) \sin\left(\frac{\Delta\varphi}{2} + \frac{k_i\pi}{2}\right) \right| \quad (9)$$

where  $k_i$  is an integer number equal to the order of the Eigen mode (e.g.,  $k_1 = 1$ ,  $k_2 = 2$ ,  $k_3 = 3$ ,  $k_4 = 4$ ,  $k_5 = 5$  for the first, second, third, fourth and fifth Eigen modes, respectively).

An overview of the accuracy of the fitting function is presented in Table IV. The necessary parameters to estimate  $V_{pred}(\Delta\varphi)$  are presented along with  $r^2$  which is the squared Pearson product moment correlation. It is apparent that the prediction function can provide a good estimation for the velocity.

TABLE IV: Overview of the fitting function accuracy.

Eigen mode ( $k_i$ )	Excitation Frequency ( $f_{meas}$ ) (kHz)	Amplitude excitation ( $A_{meas}$ ) (V)	$V_{f_{meas}}(A_{meas})$ ( $\text{m s}^{-1}$ )	$r^2$
1	108	2.5	0.28	0.9951
		5	0.94	0.9344
		7.5	1.07	0.9685
		10	1.13	0.92
2	297.4	2.5	1.25	0.9652
		5	1.50	0.9297
		7.5	1.66	0.8614
		10	1.78	0.847
3	581.8	2.5	0.63	0.9996
		5	1.20	0.9986
		7.5	1.55	0.99
		10	1.78	0.972
4	962.8	2.5	0.11	0.9977
		5	0.22	0.9993
		7.5	0.31	0.9994
		10	0.42	0.9995
5	1437.5	2.5	0.16	0.9923
		5	0.32	0.9928
		7.5	0.48	0.9939
		10	0.64	0.9943

As a result, it is possible to estimate in the reverse direction, i.e. estimate the value of  $\Delta\varphi$  from the measured velocity  $V_{measured}$  such that:

$$\Delta\varphi = k_i\pi \pm 2 \arcsin\left(\frac{V_{measured}}{V_{f_{meas}}(A_{meas})}\right) \pmod{2\pi} \quad (10)$$

Still, it is important to note that a single measured velocity will output two distinct values of  $\Delta\varphi$  and that the current operating setup does not allow any way to discriminate between them. Nevertheless, from a practical point of view, to calibrate the operation of the resonant MEMS phase comparator, at a given amplitude of excitation, it is not necessary to measure all the values of  $\Delta\varphi$ . The application of the current MEMS phase comparator thus allows the measure of the phase difference between two different excitation signals with a median  $r^2$  of 0.9926 and a standard deviation of 0.0462. Indeed, measuring the frequency response of the resonant MEMS phase comparator is sufficient, thus greatly simplifying the calibration and potential use of the resonant MEMS phase comparator.

It is also noteworthy that the value of  $r^2$  decreases when the amplitude of the excitation signal increases for the first two Eigen modes, which can be attributed to the non-linearity of the MEMS phase comparator.

#### G. Characterization using other waveforms and frequencies

The operation of the resonant MEMS phase comparator is not limited to be driven only by sinusoidal signals: other waveforms can be used. This has been experimentally validated using different types of excitation signals: a sinusoidal signal (sin), a triangular signal with 50% symmetry (ramp), a sawtooth (saw), and a square signal with 50% duty cycle (square). The influence of the variation of  $\Delta\varphi$  on these waveforms is shown in Fig. 10. For this experiment, the

amplitude ( $A$ ) and frequency of the excitation ( $f_e$ ) signal were equal to 10 V peak-to-peak and 581.8 kHz, respectively.

Interestingly, although the amplitude of all excitation signals is identical, the measured RMS velocity of the MEMS varies depending on the excitation waveform type. This is because of both the spectrum of the excitation waveform and the method used to extract the RMS velocity of the resonant MEMS phase comparator: the RMS velocity extraction involves performing an FFT operation on the acquired time-domain signal to extract the amplitude at the excitation frequency. While the amplitude of each waveform is the same (i.e. 10 V peak-to-peak), the frequency spectrum for each of these waveforms is different such that the power provided at 581.8 kHz differs.

Further experiments have also been performed to verify the operation of the MEMS outside of resonance. In this case, the amplitude of the excitation  $A$  has been set to 10 V peak-to-peak. The experimental results are shown in Fig. 11 for three frequencies. When  $f_e$  is equal to 10 kHz,  $\Delta\varphi$  does not have an appreciable effect on the RMS velocity of the resonant MEMS phase comparator. Increasing the value of  $f_e$  to 150 kHz or 1 MHz allows to detect the influence of  $\Delta\varphi$  on the RMS velocity of the resonant MEMS phase comparator. However, it must be noted that the scale of the y-axis for this figure is in  $\text{mm s}^{-1}$ , whereas the scale of the previous figures (Fig. 7 to Fig. 10) and of Table III are in  $\text{m s}^{-1}$ . This behavior is consistent with the estimation given by 9: at these frequencies, the amplitude of the frequency response is quite low. As such, while it is possible to get a response from the resonant MEMS phase comparator when used outside of its resonant bandwidth, it seems highly unlikely that practical operation will be possible as the measured RMS velocity is very low. To get around such limitation, it should be possible to use devices such as a lock-in amplifier, however this would come at the price of a significant increase of complexity of the system.

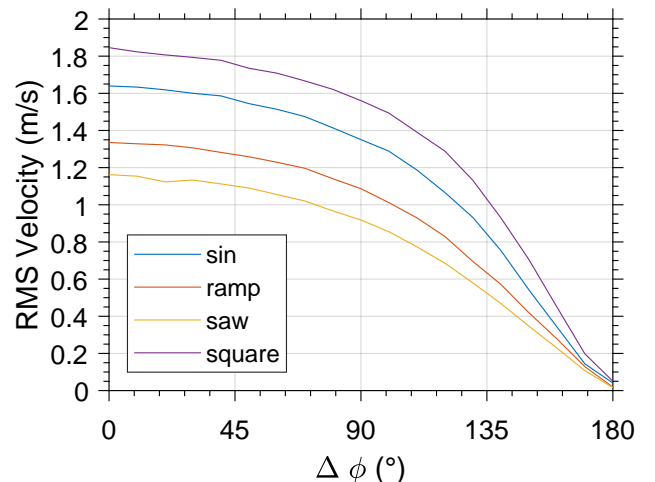


Fig. 10: Influence of the waveform type and phase difference on the velocity,  $A = 10$  V at  $f_e = 581.8$  kHz.



#### IV. DISCUSSION

As stated in the introduction, to the best knowledge of the authors, the literature on MEMS phase comparators is limited to the work presented in [25] which presents only simulation results, and to the work in [26–30] whose MEMS phase comparator consists of a power combiner with a thermoelectric power sensor. It should be noted that the work in [26–30], although operating at much higher frequencies (i.e. from 8 GHz to 12 GHz), suffers from the same limitation as this work: a phase difference can only be measured in the interval from  $0^\circ$  to  $180^\circ$ . Results from that work exhibit a trend similar to the one shown in 7, and the design is hampered by a very substantial power consumption (up to 1 W). The proposed device in this work does not consume significant power as it does not draw DC currents, and responds passively to the input signal via the piezoelectric effect.

One common limitation of IC phase comparators is the deadzone, which is defined as the maximum difference in phase between the two inputs that cannot be detected. Such a deadzone does not exist in the proposed resonant MEMS phase comparator. Nevertheless, as discernible from 9, small fluctuations of  $\Delta\varphi$  around  $0^\circ$  ( $180^\circ$ ) are more challenging to resolve than small fluctuations of  $\Delta\varphi$  around  $180^\circ$  ( $0^\circ$ ) for odd (even) Eigen modes.

It must be stated that the current prototype of the proposed resonant MEMS phase comparator is not yet suitable for use in applications such as PLLs, because the demonstrated operating frequencies are too low for typical PLL applications. Furthermore, during characterization, the excitation frequency ( $f_e$ ) and amplitude ( $A$ ) for both signals were identical, which would not be the case in normal PLL operation. However, the current performance of the prototype resonant MEMS phase comparator appears appropriate for use in Coriolis flow meters or Kelvin probe force microscopy (KPFM), given that the frequency of the excitation signals remains constant in both applications [8–10].

Finally, from a practical standpoint, the resonant MEMS

phase comparator proposed in this work is not yet usable in a system, as it requires the use of an expensive external and bulky instrument to measure the velocity: a vibrometer. Consequently, future work will aim to implement a sensing mechanism that measures the phase difference without relying on optical vibrometry. Such a sensing mechanism could rely on the piezoresistive properties of silicon, on the piezoelectric properties of AlN, on capacitive sensing or using coupled MEMS resonators. Future work will also investigate optimizing the excitation electrode topology to increase the sensitivity of the resonant MEMS phase comparator. By exploring these avenues, significant enhancements in the phase comparator's sensitivity and functionality are anticipated, potentially broadening its application scope and improving its performance in real-world scenarios. It is crucial to consider that in the practical implementation of such MEMS phase comparator, special attention has to be paid to designing the readout circuit. This design directly impacts the maximum achievable resolution of the system.

#### V. CONCLUSION

This paper has detailed the design, concept and experimental validation of a piezoelectric resonant MEMS phase comparator. Initially, a COMSOL simulation of the resonant MEMS phase comparator was introduced, followed by its design and fabrication using the commercial PiezoMUMPs MEMS fabrication technology. Furthermore, the experimental test setup and strategies employed were outlined, accompanied by recommendations for the effective characterization of MEMS phase comparators.

Experimental results showcasing the first five Eigen modes were presented, along with a proposed simple calibration method to facilitate the operation of the resonant MEMS phase comparator. The study demonstrated that the device exhibits a specific response to phase differences, enabling the extraction of phase differences between two signals through its measured velocity. Additionally, the impact of different waveform types and frequencies on the device's behavior was explored.

Looking ahead, future work will focus on enhancing the device's integrability within systems, aiming to broaden its practical use in various technological fields.

#### ACKNOWLEDGMENT

The authors would like to thank CMC Microsystems for providing the layout design tools and enabling device fabrication. The authors would also like to thank the Natural Sciences and Engineering Research Council of Canada (NSERC) and the Microsystems Strategic Alliance of Québec (ReSMiQ) for their financial support.

#### REFERENCES

- [1] Y. Zhang, J.-F. Bao, X.-Y. Li, X. Zhou, Z.-H. Wu, and X.-S. Zhang, "Fully-Differential TPoS Resonators Based on Dual Interdigital Electrodes for Feedthrough Suppression," *Micromachines*, vol. 11, no. 2, p. 119, Feb. 2020, number: 2 Publisher: Multidisciplinary Digital Publishing Institute. [Online]. Available: <https://www.mdpi.com/2072-666X/11/2/119>

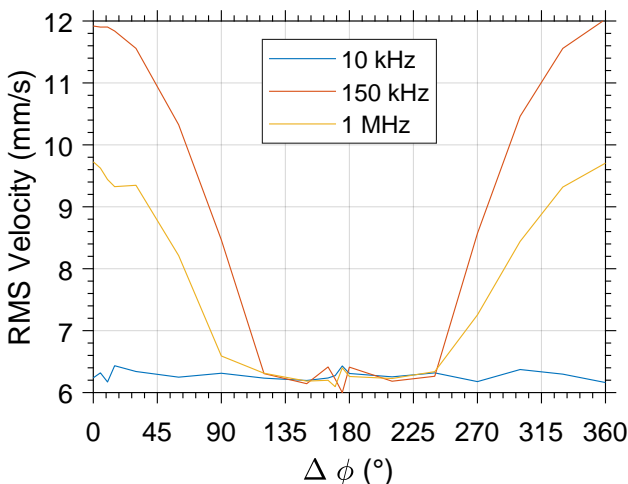
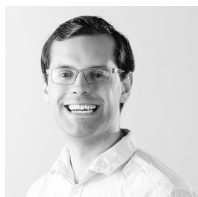


Fig. 11: Influence of  $f_e$  and  $\Delta\varphi$  on the operation of the resonant MEMS phase comparator,  $A = 10$  V.

- [2] A. Bouchaala and R. R. A. Syms, "New architectures for micromechanical coupled beam array filters," *Microsystem Technologies*, vol. 27, no. 9, pp. 3377–3387, Sep. 2021. [Online]. Available: <https://doi.org/10.1007/s00542-020-05116-w>
- [3] S. Dey, S. K. Koul, A. K. Poddar, and U. L. Rohde, "Frequency and bandwidth tunable reliable MEMS bandpass filter for 24 GHz radar applications," *International Journal of RF and Microwave Computer-Aided Engineering*, vol. 31, no. 6, p. e22662, 2021. [Online]. Available: <https://onlinelibrary.wiley.com/doi/abs/10.1002/mmce.22662>
- [4] B. Razavi, *Design of Integrated Circuits for Optical Communications*, 2nd Edition, 2nd ed., 2012.
- [5] C. Sánchez-Azqueta, C. Gimeno, C. Aldea, S. Celma, and C. Azcona, "Bang-bang phase detector model revisited," in *2013 IEEE International Symposium on Circuits and Systems (ISCAS)*, May 2013, pp. 1761–1764, iSSN: 2158-1525.
- [6] J. Haartsen and R. Dulk, "Improved Circuit Implementation of Adaptive Phase Comparators," *Electronics Letters*, vol. 24, no. 10, pp. 574–576, 1988.
- [7] K. Yoshioka, "VCO-Based Comparator: A Fully Adaptive Noise Scaling Comparator for High-Precision and Low-Power SAR ADCs," *IEEE Transactions on Very Large Scale Integration (VLSI) Systems*, vol. 29, no. 12, pp. 2143–2152, Dec. 2021, conference Name: IEEE Transactions on Very Large Scale Integration (VLSI) Systems.
- [8] C. Mills, "The consistency of pressure effects between three identical Coriolis flow meters," *Flow Measurement and Instrumentation*, vol. 80, p. 102001, Aug. 2021. [Online]. Available: <https://www.sciencedirect.com/science/article/pii/S0955598621001084>
- [9] H. Diesinger, D. Deresmes, and T. Mélin, "Noise performance of frequency modulation Kelvin force microscopy," *Beilstein Journal of Nanotechnology*, vol. 5, no. 1, pp. 1–18, Jan. 2014. [Online]. Available: <https://www.beilstein-journals.org/bjnano/articles/5/1>
- [10] W. Melitz, J. Shen, A. C. Kummel, and S. Lee, "Kelvin probe force microscopy and its application," *Surface Science Reports*, vol. 66, no. 1, pp. 1–27, Jan. 2011. [Online]. Available: <https://www.sciencedirect.com/science/article/pii/S0167572910000841>
- [11] E. Archbold, "Frequency dividing circuit and phase comparator," *Journal of Scientific Instruments*, vol. 39, no. 3, pp. 107–110, 1962.
- [12] C. Byrne, "Properties and Design of the Phase-Controlled Oscillator with a Sawtooth Comparator," *Bell System Technical Journal*, vol. 41, no. 2, pp. 559–602, 1962.
- [13] E. Kantarizis, "High-frequency phase comparator," *Proceedings of the IEEE*, vol. 53, no. 11, pp. 1784–1785, Nov. 1965, conference Name: Proceedings of the IEEE.
- [14] C. Hogge, "A self correcting clock recovery circuit," *Journal of Light-wave Technology*, vol. 3, no. 6, pp. 1312–1314, Dec. 1985.
- [15] M. Qu and Y. Hao, "A linear range extension phase frequency detector and charge pump for frequency hopping acceleration and cycle slips elimination," *Microwave and Optical Technology Letters*, vol. 64, no. 2, pp. 312–317, 2022, eprint: <https://onlinelibrary.wiley.com/doi/pdf/10.1002/mop.33117>. [Online]. Available: <https://onlinelibrary.wiley.com/doi/abs/10.1002/mop.33117>
- [16] S. Obote, Y. Sumi, N. Kitai, Y. Fukui, and Y. Itoh, "Performance improvement in a binary phase comparator type PLL frequency synthesizer," *Proceedings - IEEE International Symposium on Circuits and Systems*, vol. 4, pp. IV-419–IV-422, 1999.
- [17] Y.-S. Kim, Y. Suh, H.-J. Park, and J.-Y. Sim, "Deadzone-Minimized Systematic Offset-Free Phase Detectors," *IEICE Transactions on Electronics*, vol. E91.C, no. 9, pp. 1525–1528, 2008.
- [18] F. Nabki, K. Allidina, F. Ahmad, P.-V. Cicek, and M. N. El-Gamal, "A Highly Integrated 1.8 GHz Frequency Synthesizer Based on a MEMS Resonator," *IEEE Journal of Solid-State Circuits*, vol. 44, no. 8, pp. 2154–2168, Aug. 2009.
- [19] J.-R. Liu, C.-P. Tsai, W.-R. Du, T.-Y. Chen, J.-S. Chen, and W.-C. Li, "Vibration Mode Suppression in Micromechanical Resonators Using Embedded Anti-Resonating Structures," *Journal of Microelectromechanical Systems*, vol. 30, no. 1, pp. 53–63, 2021.
- [20] A. Robichaud, D. Deslandes, P.-V. Cicek, and F. Nabki, "A System in Package Based on a Piezoelectric Micromachined Ultrasonic Transducer Matrix for Ranging Applications," *Sensors*, vol. 21, no. 8, p. 2590, Jan. 2021. [Online]. Available: <https://www.mdpi.com/1424-8220/21/8/2590>
- [21] F. Ahmad, A. Baig, J. O. Dennis, N. H. B. Hamid, and M. H. B. Md Khir, "Characterization of MEMS comb capacitor," *Microsystem Technologies*, vol. 26, no. 4, pp. 1387–1392, Apr. 2020. [Online]. Available: <https://doi.org/10.1007/s00542-019-04671-1>
- [22] I. Zamora, E. Ledesma, A. Uranga, and N. Barniol, "Miniaturized 0.13-um CMOS Front-End Analog for AlN PMUT Arrays," *Sensors*, vol. 20, no. 4, p. 1205, Jan. 2020. [Online]. Available: <https://www.mdpi.com/1424-8220/20/4/1205>
- [23] M. Bao, "Chapter 1 - Introduction to MEMS Devices," in *Analysis and Design Principles of MEMS Devices*, M. Bao, Ed. Amsterdam: Elsevier Science, Jan. 2005, pp. 1–32. [Online]. Available: <https://www.sciencedirect.com/science/article/pii/B9780444516169500023>
- [24] X. Liu, Z. Wang, Z. Wu, Y. Gao, S. Peng, R. Ren, F. Zheng, Y. Lv, P. Yang, X. Wen, S. Xia, and C. Peng, "Enhanced Sensitivity and Stability of a Novel Resonant MEMS Electric Field Sensor Based on Closed-Loop Feedback," *IEEE Sensors Journal*, vol. 21, no. 20, pp. 22 536–22 543, Oct. 2021. [Online]. Available: <https://ieeexplore.ieee.org/document/9521911>
- [25] I. Dunk and H. Chandralahim, "Microelectromechanical Phase Detectors for Phase-Locked Loop Applications," in *2020 IEEE SENSORS*, Oct. 2020, pp. 1–4, iSSN: 2168-9229.
- [26] J. Han and X. Liao, "PLL application research of a broadband MEMS phase detector: Theory, measurement and modeling," *Solid-State Electronics*, vol. 132, pp. 6–11, Jun. 2017. [Online]. Available: <https://www.sciencedirect.com/science/article/pii/S0038110117301570>
- [27] —, "Equivalent-circuit modeling of a MEMS phase detector for phase-locked loop applications," *Solid-State Electronics*, vol. 119, pp. 5–10, May 2016. [Online]. Available: <https://www.sciencedirect.com/science/article/pii/S0038110116000204>
- [28] —, "One computer-aided equivalent circuit model of a MEMS phase detector applied in phase locked loops," in *2015 IEEE SENSORS*, Nov. 2015, pp. 1–3.
- [29] J. Han and R. Chen, "Research of a Miniaturized Broadband Mems Phase Detector and its Temperature Effect for Application in Phase-Locked Loops," in *2019 20th International Conference on Solid-State Sensors, Actuators and Microsystems Eurosensors XXXIII (TRANSDUCERS EUROSENSORS XXXIII)*, Jun. 2019, pp. 845–848, iSSN: 2167-0021.
- [30] —, "Phase-locked Loop Modelling based on Broadband Power Combiner and Capacitive MEMS Power Sensor," in *2020 IEEE SENSORS*, Oct. 2020, pp. 1–3, iSSN: 2168-9229.
- [31] H. M. Oliveira and L. V. Melo, "Huygens synchronization of two clocks," *Scientific Reports*, vol. 5, no. 1, p. 11548, Jul. 2015, bandiera\_abtest: a Cc\_license\_type: cc\_by Cg\_type: Nature Research Journals Number: 1 Primary\_atype: Research Publisher: Nature Publishing Group Subject\_term: Applied mathematics;Nonlinear phenomena Subject\_term\_id: applied-mathematics;nonlinear-phenomena. [Online]. Available: <https://www.nature.com/articles/srep11548>
- [32] M. Gratuze and F. Nabki, "Design and experimental validation of a piezoelectric resonant MEMS phase comparator," *Hilton Head*, Jun. 2022.
- [33] S. Du, Y. Jia, S.-T. Chen, C. Zhao, B. Sun, E. Arroyo, and A. A. Seshia, "A new electrode design method in piezoelectric vibration energy harvesters to maximize output power," *Sensors and Actuators A: Physical*, vol. 263, pp. 693–701, Aug. 2017. [Online]. Available: <https://www.sciencedirect.com/science/article/pii/S0924424717302194>
- [34] A. Luo, Y. Zhang, X. Guo, Y. Lu, C. Lee, and F. Wang, "Optimization of MEMS Vibration Energy Harvester With Perforated Electrode," *Journal of Microelectromechanical Systems*, vol. 30, no. 2, pp. 299–308, Apr. 2021, conference Name: Journal of Microelectromechanical Systems.
- [35] K. Roy, K. Kalyan, A. Ashok, V. Shastri, A. Jeyaseelan, A. Mandal, and R. Pratap, "A PMUT Integrated Microfluidic System for Fluid Density Sensing," *Journal of Microelectromechanical Systems*, vol. 30, no. 4, pp. 642–649, 2021.
- [36] H.-H. Cheng, S.-C. Lo, Z.-R. Huang, Y.-J. Wang, M. Wu, and W. Fang, "On the design of piezoelectric MEMS microspeaker for the sound pressure level enhancement," *Sensors and Actuators A: Physical*, vol. 306, p. 111960, May 2020. [Online]. Available: <https://www.sciencedirect.com/science/article/pii/S0924424719322691>
- [37] C. Zhao, M. H. Montaseri, G. S. Wood, S. H. Pu, A. A. Seshia, and M. Kraft, "A review on coupled MEMS resonators for sensing applications utilizing mode localization," *Sensors and Actuators A: Physical*, vol. 249, pp. 93–111, Oct. 2016. [Online]. Available: <https://www.sciencedirect.com/science/article/pii/S0924424716303454>
- [38] V. Pachkawade, "State-of-the-Art in Mode-Localized MEMS Coupled Resonant Sensors: A Comprehensive Review," *IEEE Sensors Journal*, vol. 21, no. 7, pp. 8751–8779, Apr. 2021. [Online]. Available: <https://ieeexplore.ieee.org/document/9321526>
- [39] L. Wang, C. Wang, Y. Wang, A. Qian, M. Keshavarz, B. P. Madeira, H. Zhang, C. Wang, and M. Kraft, "A Review on Coupled Bulk Acoustic Wave MEMS Resonators," *Sensors*, vol. 22, no. 10, p. 3857, Jan. 2022. [Online]. Available: <https://www.mdpi.com/1424-8220/22/10/3857>

- [40] M.-H. Bao, "Chapter 2 - Basic mechanics of beam and diaphragm structures," in *Handbook of Sensors and Actuators*, ser. Micro Mechanical Transducers, M.-H. Bao, Ed. Elsevier Science B.V., Jan. 2000, vol. 8, pp. 23–88. [Online]. Available: <https://www.sciencedirect.com/science/article/pii/S138627660080016X>
- [41] S. M. Heinrich and I. Dufour, "Fundamental Theory of Resonant MEMS Devices," in *Resonant MEMS*. John Wiley & Sons, Ltd, 2015, pp. 1–28. [Online]. Available: <https://onlinelibrary.wiley.com/doi/abs/10.1002/9783527676330.ch1>
- [42] D. L. DeVoe, "Piezoelectric thin film micromechanical beam resonators," *Sensors and Actuators A: Physical*, vol. 88, no. 3, pp. 263–272, Jan. 2001. [Online]. Available: <https://www.sciencedirect.com/science/article/pii/S0924424700005185>
- [43] G. Piazza, "Piezoelectric Resonant MEMS," in *Resonant MEMS*. John Wiley & Sons, Ltd, 2015, pp. 147–172. [Online]. Available: <https://onlinelibrary.wiley.com/doi/abs/10.1002/9783527676330.ch7>
- [44] P. Biswal, S. K. Kar, and B. Mukherjee, "Design and Optimization of High-Performance Through Hole Based MEMS Energy Harvester Using PiezoMUMPs," *Journal of Electronic Materials*, vol. 50, no. 1, pp. 375–388, Jan. 2021. [Online]. Available: <https://doi.org/10.1007/s11664-020-08528-6>
- [45] J. Pons-Nin, S. Gorreta, M. Dominguez, E. Blokhina, D. O'Connell, and O. Feely, "Design and test of resonators using PiezoMUMPS technology," in *2014 Symposium on Design, Test, Integration and Packaging of MEMS/MOEMS (DTIP)*, Apr. 2014, pp. 1–6.
- [46] A. Robichaud, D. Deslandes, P.-V. Cicek, and F. Nabki, "Electromechanical Tuning of Piecewise Stiffness and Damping for Long-Range and High-Precision Piezoelectric Ultrasonic Transducers," *Journal of Microelectromechanical Systems*, pp. 1–10, 2020.
- [47] S. Sharma, N. Kohli, J. Brière, M. Ménard, and F. Nabki, "Translational MEMS Platform for Planar Optical Switching Fabrics," *Micromachines*, vol. 10, no. 7, p. 435, Jul. 2019. [Online]. Available: <https://www.mdpi.com/2072-666X/10/7/435>
- [48] A. Cowen, G. Hames, K. Glukh, and B. Hardy, *PiezoMUMPs design handbook*. MEMSCAP Inc, 2014.
- [49] W. C. Xie, H. P. Lee, and S. P. Lim, "NORMAL MODES OF A NON-LINEAR CLAMPED-CLAMPED BEAM," *Journal of Sound and Vibration*, vol. 250, no. 2, pp. 339–349, Feb. 2002. [Online]. Available: <https://www.sciencedirect.com/science/article/pii/S0022460X01939185>
- [50] M. Gratuze, A.-H. Alameh, S. Nabavi, and F. Nabki, "Control of Spring Softening and Hardening in the Squared Daisy," *Micromachines*, vol. 12, no. 4, p. 448, Apr. 2021. [Online]. Available: <https://www.mdpi.com/2072-666X/12/4/448>



**Mathieu Gratuze** (S'19-M'22) received a Master's Degree with a major in electronics and microelectronics architecture from the École Supérieure de Chimie Physique Électronique de Lyon (CPE Lyon), Lyon, France, in 2017, and a M.Sc. degree in electrical and electronic engineering from École Centrale de Lyon (Centrale Lyon), France, in 2017. He received his Ph.D. in electrical engineering in 2022 from École de Technologie Supérieure, Montréal, Qc, Canada. He is currently working as an associate researcher with the LaCIME (Laboratoire de

Communications et d'Intégration de la MicroÉlectronique), Department of Electrical Engineering, in the École de Technologie Supérieure, Montréal, Qc, Canada. His research interests include design, modeling and characterization of piezoelectric MEMS transducers for energy harvesting and sensor applications.



**Mohammad (Michael) Kazemi** received the B.Sc. degree in mechanical engineering from Qazvin University, Qazvin, Iran, with a focus on vibrational behavior of FGM microstructures, and the M.Sc. degree in electrical engineering from École de Technologie Supérieure, Montréal, QC, Canada, in 2023. His current research interests include the design, modeling, and characterization of piezoelectric micro-electromechanical system (MEMS) resonators, transducers, and actuators for sensing applications.



**Seyedfakhreddin (Koorosh) Nabavi** (Member, IEEE) was born in Hamedan, Iran, in 1991. He received the B.Sc. degree (Hons.) in biomedical engineering (bioelectric) from the Sahand University of Technology, Tabriz, Iran, in 2013, the M.Sc. degree in electrical and electronic engineering from Ozyegin University, Istanbul, Turkey, in 2015, and the Ph.D. degree from the Memorial University of Newfoundland, St. John's, NL, Canada, in April 2019. He was a Post-Doctoral Fellow with the Department of Electrical and Computer Engineering,

McGill University, Montreal, QC, Canada. He is currently a Research Associate with École de Technologie Supérieure, Montreal, a constituent of the University of Quebec. He has published more than 40 publications and holds eight patent applications in the areas of sensors and wearable devices. His current research interests include the design and modeling of MEMS transducers and actuators for industrial and biomedical applications and the design of analog circuits, such as sensor interfaces and power management systems. He was identified as the Top Reviewer of Applied Physics Letters in 2018.



**Alexandre Robichaud** (M) received the B.Eng. degree (Hons.) in microelectronics engineering from the Université du Québec à Montréal, Canada, in 2013, the M.Eng. degree (Hons.) in electrical engineering and the Ph.D. degree (Hons.) in electrical engineering from the École de technologie supérieure, Montréal, QC, Canada, in 2015 and 2020 respectively. He has held scholarship from the Natural Sciences and Engineering Research Council of Canada (NSERC) and the Quebec Fund for Research in Nature and Technology (FQRNT). His

research interests include MEMS design and fabrication, electronic design, and ultrasound imaging.

In 2019, he joined the "Université du Québec à Chicoutimi" (UQAC), Chicoutimi, QC, Canada, where he is a Professor in Electrical Engineering.



**Paul-Vahé Cicek (M)** received the B.Eng. degree (Hons.) in electrical engineering (minor in arts) and the Ph.D. degree in electrical engineering from McGill University, Montreal, QC, Canada, in 2006 and 2016 respectively. In 2014, he joined the Université du Québec à Montréal (UQAM) as an Assistant Professor of microelectronics engineering program. As a member of the Co-design and Fabrication of Microsystems (CoFaMic) Centre, his research interests include novelty MEMS technologies and devices, monolithic integration of MEMS and VLSI

electronics, advanced packaging and encapsulation, and integrated microfluidics for lab-on-a-chip systems. To date, he has authored 15 scientific publications and holds four issued patents, with five more pending. He is currently a Professional Engineer and a member of the Ordre des Ingénieurs du Québec (OIQ). He was nominated for the excellence award from the Association des doyens des études supérieures au Québec (ADESAQ) for the quality of his Ph.D. dissertation. He has received research funding from the Natural Sciences and Engineering Research Council of Canada (NSERC), the Quebec Fund for Research in Nature and Technology (FRQNT), the Microsystems Strategic Alliance of Quebec (ReSMiQ), McGill University, and the Université du Québec à Montréal.



**Frederic Nabki (Member, IEEE)** received the B.Eng. degree (Hons.) in electrical engineering and the Ph.D. degree in electrical engineering from McGill University, Montreal, QC, Canada, in 2003 and 2010, respectively. From 2008 to 2016, he was a Professor of micro-electronics engineering with Université du Québec à Montréal (UQAM). He has been a Professor with the Department of Electrical Engineering, École de Technologie Supérieure, Montreal, since 2016. He has coauthored two book chapters and published more than 200 scientific publications. He

holds several issued patents related to MEMS, ICs, and ICs/MEMS monolithic integration. He holds or has held financial support from the Microsystems Strategic Alliance of Quebec (ReSMiQ), the Quebec Fund for Research in Nature and Technology (FRQNT), the Ministry of Economy, Science and Innovation (MESI) of Quebec, the Natural Sciences and Engineering Research Council of Canada (NSERC), and the Canada Foundation for Innovation (CFI). His current research interests include microelectromechanical systems (MEMS) and analog, radiofrequency, and mixed-signal integrated circuits (ICs), specifically focusing on the creation of next-generation MEMS processes and devices, the integration of MEMS devices with microelectronic systems, the modeling of MEMS devices, and the design of integrated circuits, such as analog to digital converters, sensor interfaces, and ultra-wideband wireless transceivers. Prof. Nabki is a member of the Communications and Micro-electronic Integration Laboratory (LACIME), ETS. He also jointly manages the Microtechnology and Microsystems Laboratory (Micro2). He was a recipient of the Governor General of Canada's Academic Bronze Medal, the UQAM Faculty of Science Early Career Research Award, the ETS Board of Directors Research Award, and the IEEE Canada J. J. Archambault Merit Award. He served as the Secretary and Treasurer of the Montreal Section of the IEEE from 2013 to 2017 and was the Local Arrangement Chair of several international IEEE conferences held in Montreal: ISCAS 2016, NEWCAS 2012 and 2018, and the Life Sciences Conference 2018. Moreover, he was a TPC Member of the NEWCAS Conference from 2013 to 2023 and the TPC co-chair in 2022.